MIT Libraries | DSpace@MIT

MIT Open Access Articles

Expanding the Dimensions of a Small, Two-Dimensional Diffraction Detector

The MIT Faculty has made this article openly available. ***Please share*** how this access benefits you. Your story matters.

Citation: Chen, Xi et al. "Expanding the Dimensions of a Small, Two-Dimensional Diffraction Detector." Microscopy and Microanalysis, 11, (August 2020): 1-6 © 2020 The Author(s)

As Published: 10.1017/s1431927620024277

Publisher: Cambridge University Press (CUP)

Persistent URL: https://hdl.handle.net/1721.1/127774

Version: Author's final manuscript: final author's manuscript post peer review, without publisher's formatting or copy editing

Terms of use: Creative Commons Attribution-Noncommercial-Share Alike

Massachusetts Institute of Technology

Expanding the dimensions of a small, two-dimensional diffraction detector

Xi Chen[a], Matthew R. Hauwiller[a], Abinash Kumar[a], Aubrey N. Penn[b], James M. LeBeau[a]

[a] *Department of Materials Science and Engineering, Massachusetts Institute of Technology, Cambridge, MA 02139*
[b] *Department of Materials Science and Engineering, North Carolina State University, Raleigh, NC 27606*

Abstract

We report an approach to expand the effective number of pixels available to small, two dimensional electron detectors. To do so, we acquire sub-sections of a diffraction pattern that are then accurately stitched together in post-processing. Using an electron microscopy pixel array detector (EMPAD) that has only 128 ×128 pixels, we show that the field of view can be expanded while achieving high reciprocal space sampling. Further, we highlight the need to properly account for the detector position (rotation) and the non-orthonormal diffraction shift axes to achieve an accurate reconstruction. Applying the method, we provide examples of spot and convergent beam diffraction patterns acquired with a pixelated detector.

Keywords:
high dynamic range, electron diffraction, diffuse scattering, direct electron cameras

---

1. Introduction

Recording electron diffraction data is perhaps the most demanding task for electron microscopy cameras and detectors. Ideally, all the electrons that impact the camera should be recorded, but this runs into limitations. For relatively low frame-rate CCDs and indirect CMOS sensors that are fiber optically coupled to a scintillator or phosphor, the incident electron current within individual diffraction spots is significant and rapidly extends beyond the detector dynamic range, which is on the order of 10^4. While this challenge can be overcome via averaging fast acquisitions (Evans and Beanland, 2014; Peters et al., 2019), the detector quantum efficiency falls off rapidly below ~100 e^-/pixel, thereby limiting acquisition rates at high frame

rates and low dose (Fan and Ellisman, 2000). Recently, however, the development of direct electron detectors has overcome these challenges and can be sorted into two major designs based on monolithic active pixel sensors and hybrid pixels (Ophus, 2019).

With superior modulation transfer functions (MTF) and detector quantum efficiencies (DQE) (McMullan et al., 2014, 2009; Bammes et al., 2012; Herzik Jr et al., 2017), direct detector designs have ushered in a new age of low-dose imaging and diffraction analysis. When applied in scanning transmission electron microscopy (STEM), the high capture rates and sensitivity have enabled one to rapidly capture the scattered electron distribution at each probe position, providing new opportunities for materials analysis. Often referred to as 4D STEM where a 2D diffraction pattern is captured at every point in a 2D image, this approach uses virtual detectors to form a variety of images after acquisition (Chen et al., 2016; Schaffer et al., 2008; Yang et al., 2015; Müller et al., 2014). Further, this method has also led to fast quantitative phase and orientation mapping (Fundenberger et al., 2003; Watanabe and Williams, 2007; Rauch and Dupuy, 2005; Rauch et al., 2010; Panova et al., 2019), strain mapping (Müller et al., 2012; Ozdol et al., 2015; Mahr et al., 2019; Pekin et al., 2018), electromagnetic field measurements (Ryll et al., 2016), and ptychographic reconstructions (Pennycook et al., 2015; Lupini et al., 2015; Jiang et al., 2018). Further , capturing all scattered electrons without saturating the detector, either in counting or charge collection mode, enables quantitative analysis of diffracted intensities on an absolute scale.

While active pixel sensor based cameras have the advantage of high pixel density (typically 16 megapixel), hybrid pixel detectors have demonstrated higher dynamic range ($>10^6$) (Tate et al., 2016; Mir et al., 2017). Furthermore, the sensitivity and dynamic range of hybrid pixel detectors provide the greatest flexibility to serve as a diffraction camera. Hybrid pixel detectors, however, offer a comparatively limited number of pixels – the Medipix3 detector is 256×256 pixels (Mir et al., 2017) while the EMPAD is 128×128 pixels (Tate et al., 2016). Furthermore, electron microscopes are rarely equipped with more than one direct electron detector. As such, being able to expand the effective pixel dimensions without the need for a separate detection unit can be extremely valuable. Although the physical size of the sensor cannot be easily increased, scripting and post-processing can provide an alternative solution, thereby widening

the range of applications without new/additional hardware. In addition, the same approach could be applied to large active sensors to further increase reciprocal-space sampling.

In this article, we demonstrate a method to increase the effective size of a small direct electron detector by shifting and combining sub-regions of reciprocal space captured with a small detector. We describe a post-acquisition process to align the sub-patterns to account for small misalignments. The sub-patterns are then combined into a single megapixel pattern, acquired with a 16 kPixel detector. This shifting approach enables the small detector to capture the electrons all the way out to the objective lens bore with a high sampling rate, with simultaneous collection of intense Bragg reflections and weak diffuse scattering. We also explore the accuracy of the reconstruction as a function of exposure time and sub-pattern overlap to help guide experimental parameters. While we demonstrate this approach using the EMPAD, this method can be applied to any other direct electron detector to increase its effective size and improve sampling.

2. Materials

Single crystal Si samples were prepared by conventional wedge polishing (Voyles et al., 2003) and thinned to electron transparency with a Fischione 1050 Ar ion mill. A Thermo Fiscer Scientific Titan G2 S/TEM equipped with a X-FEG source and operated at 200 kV was used. An EMPAD was used to collect 128 × 128 pixel diffraction pattern sub-regions with an exposure time of 1 ms. A custom Python program was used to introduce the diffraction shifts via the Thermo Fisher Scientific TEM Scripting application programming interface (API). The programs for acquisition and sub-pattern alignment can be downloaded at http://github.com/subangstrom/diffshift.

3. Methodology

The approach developed here expands the effective size of a small pixel array detector by shifting a diffraction pattern across it, Figure 1(a). For each diffraction shift, the detector then acquires a set number of frames that are then summed to form the sub-pattern for that location. The sub-patterns are then stitched together to generate the final, expanded pattern, Figure 1(b).

To implement this strategy, the microscope is scripted to shift the diffraction pattern in a grid pattern. The product of the number of frames for each shift and the frame exposure time determines the total exposure time for that sub-pattern. Moreover, by increasing the camera length, the sampling rate of reciprocal space can be increased.

In most microscopes, the diffraction shift axes are likely not orthogonal to the detector by default, as in Figure 2(a). If not accounted for, a very large overlap (more than 30% in this case) is required to fill the gaps as shown in Figure 2(b). To minimize waste, two adjacent sub-patterns should be shifted orthogonal to the detector. The angle between the shift axes and detector can be measured using the angle between matching Bragg reflections in adjacent sub-patterns. For the microscope used in this study, the rotation angle is about $22 \pm 1^{\circ}$ and results in the significant loss pixel loss, as shown in Figure 2(b). By programmatically rotating the diffraction shifts by this amount using an affine transform, the sub-patterns can be stitched directly together without significant loss or overlap as in Figure 2(c).

A custom Python interface to the TEMScripting API is used to change the microscope parameters, specifically setting the diffraction shift and camera length. A graphic user interface is used to set number of frames at each position, fraction of pattern overlap, reciprocal space range, and different shift modes (grid or annulus). For ease-of-use, the camera-length-dependent pixel size should be calibrated to accurately set the desired sub-pattern overlap. The sub-patterns are then summed and aligned post-acquisition using an a Python routine to generate the final image.

Through the flexibility of programming, alternative acquisition strategies are also readily explored. Beyond the grid described above, the diffraction pattern can also be deflected to only explore an annulus of reciprocal space, limited to within an inner and outer angle. This mode can be used to avoid the very intense central beam, which may otherwise saturate the detector in high beam current scenarios. Another benefit of this approach is that by summing many frames at each position, the signal-to-noise ratio (SNR) can be maximized (or minimized) as needed. This provides the ability to capture very weak diffuse scattering signals simultaneously with the full intensity of the Bragg reflections/direct beam.

3.1. Post-acquisition alignment

After acquisition, each sub-pattern needs to be aligned with its neighbors before stitching into the final expanded pattern. For accuracy and precision, a refinement approach is necessary due to slight diffraction shift error and rotation, likely originating from lens hysteresis. As shown in Figures 3(a,b), the alignment grid is described by two vectors, $\mathbf{V_1} = V_{1x}\mathbf{i} + V_{1y}\mathbf{j}$ and $\mathbf{V_2} = V_{2x}\mathbf{i} + V_{2y}\mathbf{j}$, that form the sub-pattern alignment grid used to generate the combined diffraction pattern. Moreover, these vectors are not guaranteed to be orthonormal and thus four independent parameters, V_{1x}, V_{1y}, V_{2x}, V_{2y}, are required to fully describe the alignment grid. It should also be noted that after correcting for the pattern rotation, the deviation from orthonormality is fairly small and does not cause significant pixel loss. For example, the difference between V_{1x} and V_{2y} is $< 10\%$, while V_{1y} and V_{2x} are only slightly larger than zero, which corresponds to a loss of less than 5 pixels over the entire pattern. The two alignment grid vectors are determined using a set of sub-patterns, namely red those that contain diffraction spots, disks, or other strong features. Furthermore, the parameter refinement step requires sub-pixel precision, which is necessary as the diffraction shift step size is unlikely to be an exact integer number of pixels.

Since the two alignment grid vectors are independent, they are fit separately using a sub-pattern and its left-right neighbors (for $\mathbf{V_1}$) or the up-down neighbors (for $\mathbf{V_2}$). A non-linear least squares fit is employed to minimize the difference between overlapped regions, normalizing with respect to the integrated intensity. A mask smaller than the overlapped region, Figure 3(c), is used to ensure that the size of the output is unchanged during the fitting process. To improve precision, multiple sub-patterns can be selected for alignment where each selected sub-pattern and its nearest neighbors are used to calculate the alignment grid vectors. The subsequent set of vectors are then averaged together.

While fit results for consecutive full-pattern acquisitions are fairly stable, less than 0.7% variation, V_{1x} and V_{2y} are found to vary over time – usually within 10% . Additionally, we have also found that (V_{1y}, V_{2x}) vary within 1-5 pixels over time. Therefore, $\mathbf{V_1}$ and $\mathbf{V_2}$ should be determined for each reconstruction to ensure accuracy. The alignment fit, however, is not particularly sensitive on the initial estimates of the alignment grid vectors. For example, the vec-

tor components converge to the same values if the starting points are within -10 to 10 pixels, which is a significant fraction of the sub-pattern size. As the deviation from orthonormality is subtle, it is recommended that the initial condition for V_{1y} and V_{2x} be set to zero in most cases. Moreover, the alignment converges within 0.5 seconds for one selected sub-pattern and its four nearest neighbors.

Using the average alignment vectors determined using multiple overlapped regions, the other sub-patterns are then stitched together. To do so, each sub-pattern is first zero-padded to the size of the final image. An affine transformation is then applied to sub-pixel shift the sub-pattern to it final position, applying bi-linear interpolation. The shifted sub-patterns are eroded using a 5 square structuring element to remove shifting edge effects. The sub-patterns are then summed into the expanded, final pattern.

Due to the large dynamic range, it is possible to over-run the 32-bit format of the original raw data, particularly at the direct beam location. To avoid this, the sub-patterns are converted to 64-bit dataset before summing. Furthermore, the final pattern is normalized using a matrix where the values represent the number of sub-patterns contributing to each pixel. To form this matrix, each aligned sub-pattern is reduced to a binary image where all non-zero pixels are set equal to unity. After summing these binary sub-patterns, the integer counts, Figure 3(a), are used to normalize the final pattern on a pixel-wise basis. The result is a seamless reconstruction of a finely sampled diffraction pattern over a large range of reciprocal space, but captured using a 128×128 pixel detector. After normalizing, the pattern can be downcast to a 32-bit image format if needed.

4. Results and Discussion

To highlight applications and benefits of the approach outlined above, $\langle 111 \rangle$ Si diffraction patterns are shown in Figure 4. In Figure 4(a), fine details within the CBED disks and the Kikuchi bands are captured at the same time as shown on both linear and log intensity scales. Notably, the Kikuchi bands and objective lens bore edge both remain smooth and continuous. With respect to alignment accuracy, this observation indicates there is little error introduced from shifting the diffraction pattern. An enlargement of the central sub-pattern region before and

after stitching exhibits negligible difference as shown in Figure 4(b). With 10% sub-pattern overlap and a 9×9 grid of sub-patterns, the resulting pattern is approximately 1024×1024 pixels. In other words, a 16 kPixel detector can be transformed into a MPixel detector with single electron sensitivity and 1,000,000:1 dynamic range using this approach.

By changing the camera length and the number of sub-patterns, the reciprocal space sampling range can be tuned to specific applications. As highlighted in Figure 4(c, d), the diffraction pattern can be finely sampled (0.6509 mrad/pixel) out to the objective lens bore with the EMPAD pixel detector. Moreover, the largest camera length on the microscope used in this study was 4.1 m, which equates to a reciprocal space sampling rate of 0.1646 mrad/pixel. It is also important to note that the number of sub-patterns required will depend on the desired angular range to be captured.

Spot patterns can also be acquired with this approach as shown for in Figures 5(a,b). By averaging a sufficient number of frames, the high dynamic range and SNR captures the intensity of the Bragg reflections and the very weak diffuse scattering, about 6 orders as shown in Figure 5. It is important to note that the signal does not saturate anywhere across the entire pattern, with the fine details of the disk and background captured. Thus, the approach outlined here enables a small, high sensitivity detector to capture the scattered intensity with high sampling, enabling the possibility of quantitative diffuse electron scattering studies similar to those carried out using neutrons and X-rays (Holt et al., 1999; Xu and Chiang, 2005; Axe and Shirane, 1973).

4.1. Reconstruction Accuracy

To quantify the accuracy of the reconstruction, the distance between mirrored lowest order reflections, e.g. $g_{2\bar{2}0}$ and $g_{\bar{2}20}$, are measured using the pattern in Figure 5(a). In the ideal case, the ratio of these lowest order distances are all equal to 1.0. Here, these ratios are: $g_{0\bar{2}2}/g_{02\bar{2}}$ = 1.01, $g_{\bar{2}02}/g_{20\bar{2}}$ = 1.02, $g_{\bar{2}20}/g_{2\bar{2}0}$ = 0.98. Similar errors are found when using the same approach to measure a spot diffraction pattern captured in a single 4 MPixel image with a CCD.

In addition, the angles between consecutive systematic rows are $g_{0\bar{2}2}\angle g_{\bar{2}02}$ = 59.96° , $g_{\bar{2}02}\angle g_{\bar{2}20}$ = 59.93°, and $g_{\bar{2}20}\angle g_{02\bar{2}}$ = 60.16° as determined using the projective standard deviation (Sang

et al., 2014). The largest deviation from the expected value is less than 0.2° or 0.34% relative error, again consistent with spot analysis of a pattern captured with a high pixel density detector.

4.2. Correction Parameter Stability

As discussed in Section 3, the central sub-patterns and their nearest neighbors are used to determine the average alignment vectors, $\mathbf{V_1}, \mathbf{V_2}$. These vectors are then applied to the align the rest of the sub-patterns in the set. The procedure is valid under the assumption that the overlap and the shift corrections are the same for sub-patterns across the entire diffraction pattern. To determine the validity of this assumption, 81 sub-patterns of a $\langle 111 \rangle$ Si CBED pattern are collected at a 1.2 m camera length (0.6509 mrad/pixel) and used to determine the alignment vector components as shown in Figure 6. The components are stable when using the sub-patterns near the direct beam where there are more features in the overlapped regions. For the 21 patterns at the center, the standard deviations of the vector components are 0.126 mrad for V_{1x}, 0.111 mrad for V_{1y}, 0.149 mrad for V_{2x}, and 0.081 mrad for V_{2y}, indicating sub-pixel precision.

When sub-patterns far from the direct beam are used, see blue triangles in Figure 6(c), the vector components do not converge to stable values. This is likely the result of fewer strong features in those sub-patterns, which decreases the sensitivity of the least squares fit to small changes in the alignment grid. Furthermore, there are fewer electrons scattered at these higher angles, thus resulting in a lower SNR, further degrading fit stability. Thus to maintain the final accuracy of the reconstructed diffraction information, sub-patterns near the center (or with more features) are required to determine the alignment grid.

4.3. Effect of Exposure and Overlap on Correction Parameter Estimation

The exposure time (or more precisely the SNR), sub-pattern overlap, and the reciprocal space range all determine the time needed to capture the full pattern. While the total time increases with longer exposures and larger overlap, the alignment accuracy decreases as these parameters are decreased. Thus, optimizing the sub-pattern overlap and exposure are critical to provide the largest range while at the same time ensuring alignment accuracy.

To examine the influence of overlap, the nine central sub-patterns(together with their nearest neighbors) in Figure 6(a) are used to fit the alignment vector components. As shown in Figure 7, the components vary significantly when the overlap is below 10% (large standard deviation). As the overlap increase above 10%, the fit converges to a stable values for each component (deviation less than 0.1%). When the overlap is more than 10%, the vector component standard deviations are 0.021 mrad for V_{1x}, 0.012 mrad for V_{1y}, 0.008 mrad for V_{2x}, and 0.009 mrad for V_{2y}. Based on these results, a minimum overlap of 10% is required for the procedure outlined above, but feature-rich patterns can likely reduce this further.

The exposure time and electron dose rate determine the final SNR. The SNR can be measured using consecutive sub-patterns acquired at the same shift position via the image correlation method described in Ref. Huang et al. (2009) . To explore the influence of SNR on the stability of the pattern alignment, the electron dose rate is assumed to be constant during a sub-pattern acquisition so that the total dose can be linearly varied by summing frames. As shown in Figure 7(d), the SNR increases with exposure time and quickly saturates after 1 s. Therefore, increasing the exposure time beyond this point yields diminishing returns. It is also important to note that in general the specific exposure time to achieve a certain SNR will depend on the thickness of the sample and the features available within the pattern. Here, the capture rate is ~1000 fps.

The alignment vector component fits as a function of SNR are shown in Figure 7(b). When only 20 frames of a sub-pattern are averaged and exbiting poor SNR, such as that in Figure 7(c), the vector components exhibit a large standard deviation. Summing additional frames rapidly converges the components to stable values, minimally varying with respect to longer acquisitions, i.e. those sub-patterns with exposure times longer than 1.5 s or SNR > 130. When compared the longest acquisition time, the vector component fit error is < 0.5% for a sub-pattern SNR > 178, which corresponds to 820 frames or 0.82 s, shown in Figure 7(c).

The diffraction pattern in Figure 7 is sampled with 40% overlap at an exposure of 0.82 s and covers a 500 mrad span. To capture details, a 9 × 9 grid of sub-patterns is used. When accounting for the total exposure time, there is only a slight delay of 3-5 ms between diffraction shifts which is limited by the microscope optics. Without further integration between the software

and microscope hardware, additional time is needed to write the data to disk, which can vary from fractions of a second to several seconds depending on the size of data. Direct access to the camera memory and/or multi-threading would resolve this time delay in future iterations. Even so, the dose can be minimized by blanking the beam while saving a sub-pattern dataset.

Not including the time to save data, the total acquisition time for the pattern in Figure 7 is estimated to be about 67s. While the sub-pattern overlap is 40%, this is unnecessary for accurate alignment as described above. Thus, if the minimum overlap (10%) is used, only 36 shifts are needed for a total pattern acquisition time of about 30 s. In addition, sample drift can limit positional accuracy of long (> 60 s) acquisitions, i.e. 4D STEM datasets. While drift correction is not implemented here, this could be included by capturing an HAADF STEM image for every row of sub-patterns. By cross correlating this image as a functiont of time to measure the drift, compensation by beam shifts or stage movements could be applied during acquisition.

5. Conclusions

While small pixel array detectors limit the reciprocal space region that can be finely sampled at any given time, the method described here enables sub-patterns to be accurately recombined into a single, large pattern. The available detection region and sampling rate are then only limited by the objective lens bore and maximum camera length. Furthermore, the post-acquisition alignment procedure is fast, stable, and efficient. With the high dynamic range and single electron sensitivity of a direct electron detector, the approach has the potential to enable quantitative diffraction analysis on an absolute intensity scale that spans from the very weak diffuse scattering to the intense Bragg reflections. With a fast, small detector, applications for the approach also include expanding reciprocal space sampling of 4D STEM datasets to improve strain or electromagnetic field measurement precision.

6. Acknowledgement

We acknowledge support for this work from the Air Force Office of Scientific Research (FA9550-17-1-0225). This work was performed in part at the Analytical Instrumentation Facility (AIF) at

North Carolina State University, which is supported by the State of North Carolina and the National Science Foundation (award number ECCS-1542015). This work made use of instrumentation at AIF acquired with support from the National Science Foundation (DMR-1726294). The AIF is a member of the North Carolina Research Triangle Nanotechnology Network (RTNN), a site in the National Nanotechnology Coordinated Infrastructure (NNCI)

7. References

AXE, J. AND SHIRANE, G. 1973. Inelastic-neutron-scattering study of acoustic phonons in nb 3 sn. *Physical Review B* 8:1965.

BAMMES, B. E., ROCHAT, R. H., JAKANA, J., CHEN, D.-H., AND CHIU, W. 2012. Direct electron detection yields cryo-em reconstructions at resolutions beyond 3/4 nyquist frequency. *Journal of structural biology* 177:589–601.

CHEN, Z., WEYLAND, M., ERCIUS, P., CISTON, J., ZHENG, C., FUHRER, M., D'ALFONSO, A., ALLEN, L., AND FINDLAY, S. 2016. Practical aspects of diffractive imaging using an atomic-scale coherent electron probe. *Ultramicroscopy* 169:107–121.

EVANS, K. AND BEANLAND, R. 2014. High dynamic range electron imaging: The new standard. *Microscopy and Microanalysis* 20:1601–1604.

FAN, G. Y. AND ELLISMAN, M. H. 2000. Digital imaging in transmission electron microscopy. *Journal of Microscopy* 200:1–13.

FUNDENBERGER, J.-J., MORAWIEC, A., BOUZY, E., AND LECOMTE, J.-S. 2003. Polycrystal orientation maps from tem. *Ultramicroscopy* 96:127–137.

HERZIK JR, M. A., WU, M., AND LANDER, G. C. 2017. Achieving better-than-3-å resolution by single-particle cryo-em at 200 kev. *Nature methods* 14:1075.

HOLT, M., WU, Z., HONG, H., ZSCHACK, P., JEMIAN, P., TISCHLER, J., CHEN, H., AND CHIANG, T.-C. 1999. Determination of phonon dispersions from x-ray transmission scattering: The example of silicon. *Physical review letters* 83:3317.

HUANG, X., MIAO, H., STEINBRENER, J., NELSON, J., SHAPIRO, D., STEWART, A., TURNER, J., AND JACOBSEN, C. 2009. Signal-to-noise and radiation exposure considerations in conventional and diffraction x-ray microscopy. *Optics express* 17:13541–13553.

JIANG, Y., CHEN, Z., HAN, Y., DEB, P., GAO, H., XIE, S., PUROHIT, P., TATE, M. W., PARK, J., GRUNER, S. M., ELSER, V., AND MULLER, D. A. 2018. Electron ptychography of 2d materials to deep sub-ångström resolution. *Nature* 559:343–349.

LUPINI, A. R., CHI, M., KALININ, S. V., BORISEVICH, A. Y., IDROBO, J. C., AND JESSE, S. 2015. Ptychographic imaging in an aberration corrected stem. *Microscopy and Microanalysis* 21:1219–1220.

MAHR, C., MÜLLER-CASPARY, K., RITZ, R., SIMSON, M., GRIEB, T., SCHOWALTER, M., KRAUSE, F. F., LACKMANN, A., SOLTAU, H., WITTSTOCK, A., ET AL. 2019. Influence of distortions of recorded diffraction patterns on strain analysis by nano-beam electron diffraction. *Ultramicroscopy* 196:74–82.

MCMULLAN, G., FARUQI, A., CLARE, D., AND HENDERSON, R. 2014. Comparison of optimal performance at 300 kev of three direct electron detectors for use in low dose electron microscopy. *Ultramicroscopy* 147:156–163.

MCMULLAN, G., FARUQI, A., HENDERSON, R., GUERRINI, N., TURCHETTA, R., JACOBS, A., AND VAN HOFTEN, G. 2009. Experimental observation of the improvement in mtf from backthinning a cmos direct electron detector. *Ultramicroscopy* 109:1144–1147.

MIR, J. A., CLOUGH, R., MACINNES, R., GOUGH, C., PLACKETT, R., SHIPSEY, I., SAWADA, H., MACLAREN, I., BALLABRIGA, R., MANEUSKI, D., O'SHEA, V., MCGROUTHER, D., AND KIRKLAND, A. I. 2017. Characterisation of the medipix3 detector for 60 and 80kev electrons. *Ultramicroscopy* 182:44–53.

MÜLLER, K., KRAUSE, F. F., BÉCHÉ, A., SCHOWALTER, M., GALIOIT, V., LÖFFLER, S., VERBEECK, J., ZWECK, J., SCHATTSCHNEIDER, P., AND ROSENAUER, A. 2014. Atomic electric fields revealed by a quantum mechanical approach to electron picodiffraction. *Nature communications* 5:1–8.

MÜLLER, K., RYLL, H., ORDAVO, I., IHLE, S., STRÜDER, L., VOLZ, K., ZWECK, J., SOLTAU, H., AND ROSENAUER, A. 2012. Scanning transmission electron microscopy strain measurement from millisecond frames of a direct electron charge coupled device. *Applied Physics Letters* 101:212110.

OPHUS, C. 2019. Four-dimensional scanning transmission electron microscopy (4d-stem): From scanning nanodiffraction to ptychography and beyond. *Microscopy and Microanalysis* 25:563–582.

OZDOL, V., GAMMER, C., JIN, X., ERCIUS, P., OPHUS, C., CISTON, J., AND MINOR, A. 2015. Strain mapping at nanometer resolution using advanced nano-beam electron diffraction. *Applied Physics Letters* 106:253107.

PANOVA, O., OPHUS, C., TAKACS, C. J., BUSTILLO, K. C., BALHORN, L., SALLEO, A., BALSARA, N., AND MINOR, A. M. 2019. Diffraction imaging of nanocrystalline structures in organic semiconductor molecular thin films. *Nature materials* p. 1.

PEKIN, T. C., GAMMER, C., CISTON, J., OPHUS, C., AND MINOR, A. M. 2018. In situ nanobeam electron diffraction strain mapping of planar slip in stainless steel. *Scripta Materialia* 146:87–90.

PENNYCOOK, T. J., LUPINI, A. R., YANG, H., MURFITT, M. F., JONES, L., AND NELLIST, P. D. 2015. Efficient phase contrast imaging in stem using a pixelated detector. part 1: Experimental demonstration at atomic resolution. *Ultramicroscopy* 151:160–167.

PETERS, J. J. P., SANCHEZ, A. M., WALKER, D., WHATMORE, R., AND BEANLAND, R. 2019. Quantitative high-dynamic-range electron diffraction of polar nanodomains in pb2sctao6. *Advanced Materials* 31:1806498.

RAUCH, E. AND DUPUY, L. 2005. Rapid spot diffraction patterns idendification through template matching.

Archives of Metallurgy and Materials 50:87–99.

RAUCH, E. F., PORTILLO, J., NICOLOPOULOS, S., BULTREYS, D., ROUVIMOV, S., AND MOECK, P. 2010. Automated nanocrystal orientation and phase mapping in the transmission electron microscope on the basis of precession electron diffraction. *Zeitschrift für Kristallographie International journal for structural, physical, and chemical aspects of crystalline materials* 225:103–109.

RYLL, H., SIMSON, M., HARTMANN, R., HOLL, P., HUTH, M., IHLE, S., KONDO, Y., KOTULA, P., LIEBEL, A., MÜLLER-CASPARY, K., ET AL. 2016. A pnccd-based, fast direct single electron imaging camera for tem and stem. *Journal of Instrumentation* 11:P04006.

SANG, X., ONI, A. A., AND LEBEAU, J. M. 2014. Atom Column Indexing: Atomic Resolution Image Analysis Through a Matrix Representation. *Microsc. Microanal.* 20:1764–1771.

SCHAFFER, B., GSPAN, C., GROGGER, W., KOTHLEITNER, G., AND HOFER, F. 2008. Hyperspectral imaging in tem: New ways of information extraction and display. *Microscopy and microanalysis* 14:70–71.

TATE, M. W., PUROHIT, P., CHAMBERLAIN, D., NGUYEN, K. X., HOVDEN, R., CHANG, C. S., DEB, P., TURGUT, E., HERON, J. T., SCHLOM, D. G., ET AL. 2016. High dynamic range pixel array detector for scanning transmission electron microscopy. *Microscopy and Microanalysis* 22:237–249.

VOYLES, P., GRAZUL, J., AND MULLER, D. 2003. Imaging individual atoms inside crystals with ADF-STEM. *Ultramicroscopy* 96:251–273.

WATANABE, M. AND WILLIAMS, D. 2007. Development of diffraction imaging for orientation analysis of grains in scanning transmission electron microscopy. *Microscopy and Microanalysis* 13:962–963.

XU, R. AND CHIANG, T. C. 2005. Determination of phonon dispersion relations by x-ray thermal diffuse scattering. *Zeitschrift für Kristallographie-Crystalline Materials* 220:1009–1016.

YANG, H., JONES, L., RYLL, H., SIMSON, M., SOLTAU, H., KONDO, Y., SAGAWA, R., BANBA, H., MACLAREN, I., AND NELLIST, P. 2015. 4d stem: High efficiency phase contrast imaging using a fast pixelated detector. *In* Journal of Physics: Conference Series, volume 644, p. 012032. IOP Publishing.

List of Figures

1 (a) Schematic of shifting each sub-section of the diffraction pattern across a small, high sensitivity detector. (b) The combination of these patterns can capture a large portion of reciprocal space while maintaining high sampling. 15

2 (a) Diffraction shift axes are not likely to be aligned to the detector, requiring (b) each sub-pattern to be significantly overlapped with neighbors to avoid data gaps. (c) Correcting the shift axes for rotation significantly reduces the amount of overlap needed. 16

3 (a) Schematic of the vectors $\mathbf{V_1}$ and $\mathbf{V_2}$ that expand into a grid of positions to (b) align the sub-patterns. 17

4 (a) Si ⟨111⟩ CBED pattern shown on different intensity scales. (b) Detail image of the sub-pattern region indicated in (a) before and after stitching. (c, d) same as (a,b) but acquired at lower camera length to capture a larger region of reciprocal space. 18

5 (a) Spot pattern of Si ⟨111⟩ and a (b) sub-pattern region showing that weak thermal diffuse scattering is captured at the same time as the Bragg reflections and direct beam. (c) Line profile through the direct beam and Bragg reflections. (d) Line profile across Bragg reflections and thermal diffuse scattering. 19

6 (a) Sub-patterns of a ⟨111⟩ Si diffraction pattern before alignment. (b) Inner and outer regions for the different sub-patterns in (a). (c) Alignment vector components that result from fitting each sub-pattern where the triangles (blue) and circles (red) correspond to the outer and inner sub-patterns in (b), respectively. . . . 20

7 Alignment vector components as a function of sub-pattern (a) overlap and (b) exposure. The mean (y direction – triangles, x direction – dots) and standard deviation (denoted by shaded region in (a) and (b)) of each component determined using the 9 central sub-patterns. (c) Sub-pattern average using 20 and 820 frames.(d) the signal-to-noise ratio as a function of exposure time. 21

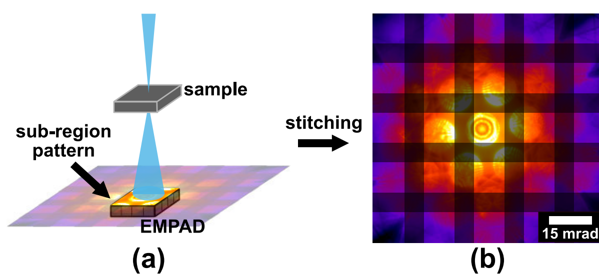

Figure 1: (a) Schematic of shifting each sub-section of the diffraction pattern across a small, high sensitivity detector. (b) The combination of these patterns can capture a large portion of reciprocal space while maintaining high sampling.

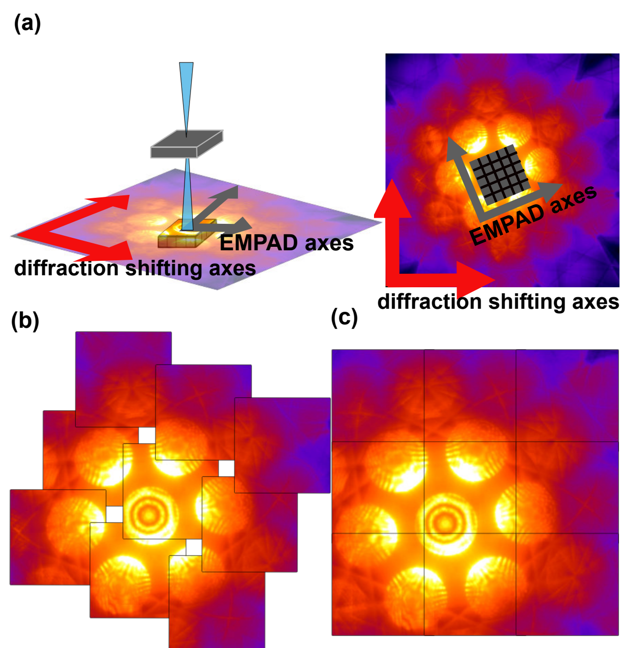

Figure 2: (a) Diffraction shift axes are not likely to be aligned to the detector, requiring (b) each sub-pattern to be significantly overlapped with neighbors to avoid data gaps. (c) Correcting the shift axes for rotation significantly reduces the amount of overlap needed.

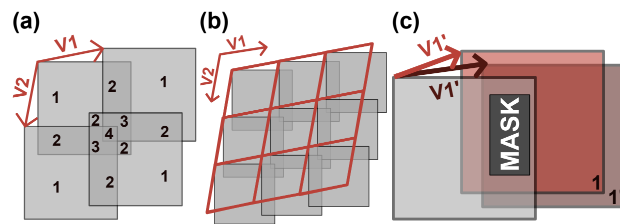

Figure 3: (a) Schematic of the vectors $\mathbf{V_1}$ and $\mathbf{V_2}$ that expand into a grid of positions to (b) align the sub-patterns. Alignment grid vector components are determined using neighboring sub-patterns to minimize the difference between overlapped regions as in (c).

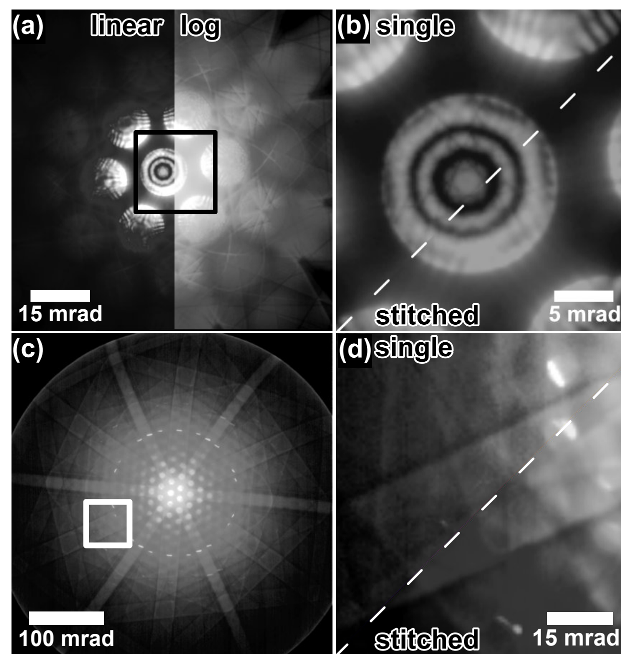

Figure 4: (a) Si ⟨111⟩ CBED pattern shown on different intensity scales. (b) Detail image of the sub-pattern region indicated in (a) before and after stitching. (c, d) same as (a,b) but acquired at lower camera length to capture a larger region of reciprocal space.

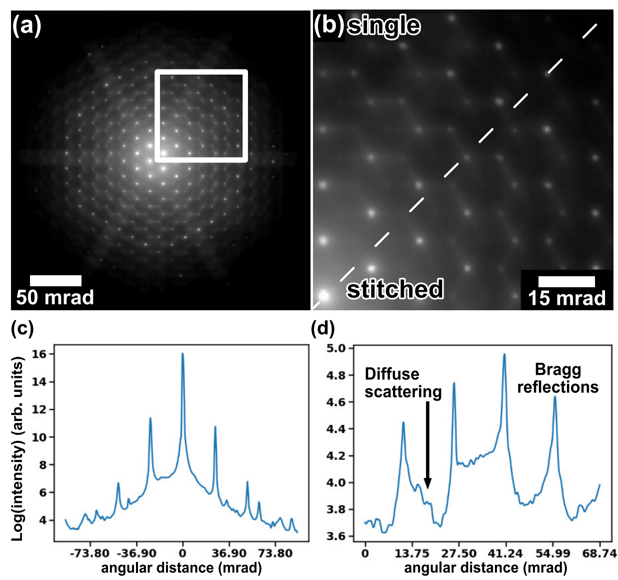

Figure 5: (a) Spot pattern of Si ⟨111⟩ and a (b) sub-pattern region showing that weak thermal diffuse scattering is captured at the same time as the Bragg reflections and direct beam. (c) Line profile through the direct beam and Bragg reflections. (d) Line profile across Bragg reflections and thermal diffuse scattering.

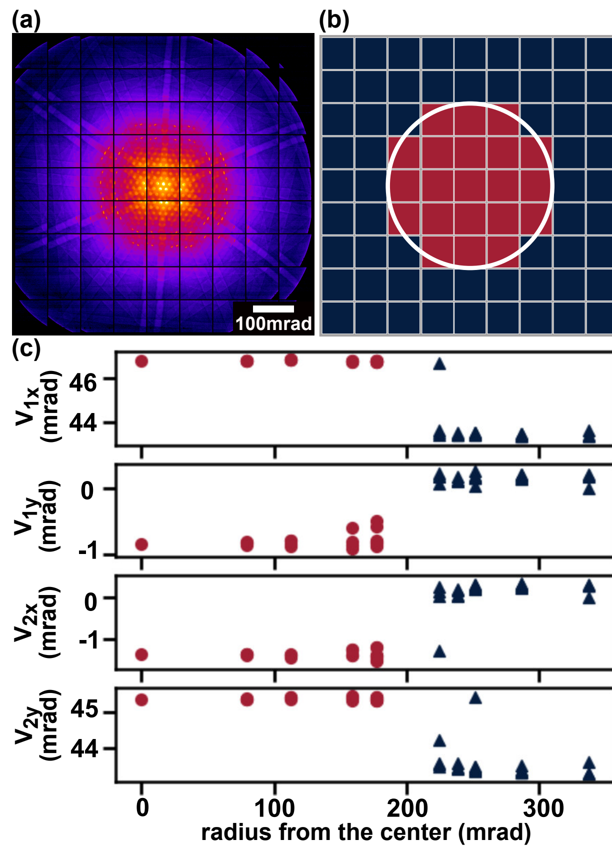

Figure 6: (a) Sub-patterns of a ⟨111⟩ Si diffraction pattern before alignment. (b) Inner and outer regions for the different sub-patterns in (a). (c) Alignment vector components that result from fitting each sub-pattern where the triangles (blue) and circles (red) correspond to the outer and inner sub-patterns in (b), respectively.

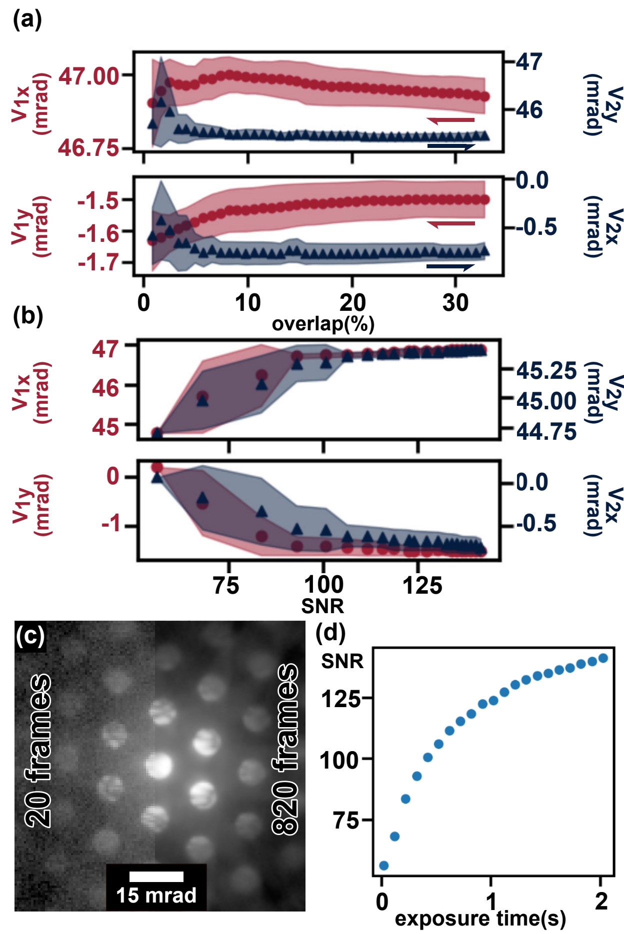

Figure 7: Alignment vector components as a function of sub-pattern (a) overlap and (b) exposure. The mean (y direction – triangles, x direction – dots) and standard deviation (denoted by shaded region in (a) and (b)) of each component determined using the 9 central sub-patterns. (c) Sub-pattern average using 20 and 820 frames.(d) the signal-to-noise ratio as a function of exposure time.